

LETTER TO THE EDITOR

FAUST XV. A disk wind mapped by CH₃OH and SiO in the inner 300 au of the NGC 1333 IRAS 4A2 protostar.

M. De Simone^{1,2}, L. Podio², L. Chahine³, C. Codella^{2,3}, C. J. Chandler⁴, C. Ceccarelli³, A. López-Sepulcre^{3,5}, L. Loinard^{6,7}, B. Svoboda⁴, N. Sakai⁸, D. Johnstone^{9,10}, F. Ménard³, Y. Aikawa¹¹, M. Bouvier¹², G. Sabatini², A. Miotello¹, C. Vastel¹³, N. Cuello³, E. Bianchi¹⁴, P. Caselli¹⁵, E. Caux¹³, T. Hanawa¹⁶, E. Herbst¹⁷, D. Segura-Cox^{15,18}, Z. Zhang⁸, and S. Yamamoto¹⁹

(Affiliations can be found after the references)

May 1, 2024

ABSTRACT

Context. Understanding the connection between outflows, winds, accretion and disks in the inner protostellar regions is crucial for comprehending star and planet formation process.

Aims. We aim to explore the inner 300 au of the protostar IRAS 4A2 as part of the ALMA FAUST Large Program.

Methods. We analysed the kinematical structures of SiO and CH₃OH emission with 50 au resolution.

Results. The emission arises from three zones: i) a very compact and unresolved region (<50 au) dominated by the ice sublimation zone, at ± 1.5 km s⁻¹ with respect to v_{sys} , traced by methanol; ii) an intermediate region (between 50 au and 150 au) traced by both SiO and CH₃OH, between 2 and 6 km s⁻¹ with respect to v_{sys} , with an inverted velocity gradient (with respect to the large scale emission), whose origin is not clear; iii) an extended region (> 150 au) traced by SiO, above 7 km s⁻¹ with respect to v_{sys} , and dominated by the outflow. In the intermediate region we estimated a CH₃OH/SiO abundance ratio of about 120–400 and a SiO/H₂ abundance of 10⁻⁸. We explored various possibilities to explain the origin of this region such as, rotating disk/inner envelope, jet on the plane of the sky/precessing, wide angle disk wind.

Conclusions. We propose that CH₃OH and SiO in the inner 100 au probe the base of a wide-angle disk wind. The material accelerated in the wind crosses the plane of the sky, giving rise to the observed inverted velocity gradient, and sputtering the grain mantles and cores releasing CH₃OH and SiO. This is the first detection of a disk wind candidate in SiO, and the second ever in CH₃OH.

Key words. Stars: formation — ISM: chemical abundances — ISM: protostars — ISM: molecules — ISM: astrochemistry — ISM: young stellar objects

1. Introduction

Solar-like stars form from an accreting object deeply embedded in a dense envelope that drives bipolar jets. To allow the accretion from the disk onto the protostar, the angular momentum is extracted from the disk by jets/outflows or disk winds (e.g., Shu et al. 1987). Understanding the accretion and ejection mechanisms and their impact on the physical and chemical structure of protostars is of paramount importance to our comprehension of the evolution of the forming stellar/planetary system.

Low-mass Class 0 protostars ($\sim 10^4$ yr; Andre et al. 2000) are the most studied objects to investigate both the accreting region and the molecular outflows. Some protostars hosts hot (>100 K), compact (<100 au), dense ($> 10^7$ cm⁻³) regions rich in iCOMS (interstellar Complex Organic Molecules; Herbst & Van Dishoeck 2009; Ceccarelli et al. 2017), where the ice mantle sublimation dominates the chemistry (called hot corinos; Ceccarelli 2004). However, not every protostar possesses a hot corino (e.g., De Simone et al. 2017; Belloche et al. 2020; Bouvier et al. 2022; Yang et al. 2020; De Simone et al. 2020; De Simone et al. 2022a), and their physical and chemical structure is still not clear. Among the few known hot corinos, only a handful are spatially resolved (SVS13-A, HH212, IRAS 16293A, B335; Bianchi et al. 2023; Lee et al. 2022a; Maureira et al. 2022; Okoda et al. 2022). Here, the iCOMS emission seems to probe different layers of the hot corino or selected regions associated to accretion shocks and/or hot spots.

On the other hand, jets and outflows driven by protostellar sources have been extensively studied, especially at scales larger than 500 au (e.g., Ray et al. 2007; Arce et al. 2007; Frank et al. 2014). However, their origin is still debated. Models predict that magneto centrifugal mechanisms extracts material from the disk from two regions: close to the dust truncation radius by a stellar magnetosphere (X-wind models: Shu et al. 1994; Arce et al. 2007; Shang et al. 2007), and a wider range of radii outside this dust truncation radius (disk-wind models: Blandford & Payne 1982; Konigl & Pudritz 2000; Tsukamoto et al. 2022).

These winds have been considered as a solution to the angular momentum problem in the inner 50 au of the disks (e.g., Pascucci et al. 2023). However, only a handful of resolved disk winds observations are available (e.g., Tabone et al. 2017; Zhang et al. 2018; Louvet et al. 2018; de Valon et al. 2020; Lee et al. 2021a; López-Vázquez et al. 2024). These type of observations provide crucial information (e.g., geometry, kinematical and chemical structure) to constrain disk wind models, and to retrieve their origin, and the interplay between accretion and ejection mechanisms.

In this Letter we explore the inner 300 au of the IRAS 4A2 protostar as part of the ALMA FAUST¹ (Codella et al. 2021) Large Program in SiO and CH₃OH. We study the kinematics of the gas in the transition zone between a possible disk and the

¹ Fifty AU Study of the chemistry in the disk/envelope systems of Solar-like protostars; <http://faust-alma.riken.jp>.

outflowing material, and present, for the first time, a wide disk wind candidate for NGC 1333 IRAS 4A2 traced by SiO.

The target: NGC 1333 IRAS 4A is a very well studied system in Perseus (~ 300 pc away; Zucker et al. 2018). It is composed of two protostars: IRAS 4A1 (4A1 hereinafter), the brightest in mm continuum, and IRAS 4A2 (4A2 hereinafter), separated by about $1''.8$ (about 540 au; Looney et al. 2000; Santangelo et al. 2015; López-Sepulcre et al. 2017; Tobin et al. 2018). They are surrounded by a common envelope of about $8 M_{\odot}$ (Maury et al. 2019) and have a total bolometric luminosity of about $9 L_{\odot}$ (Kristensen et al. 2012; Karska et al. 2013). Note that the system is also known to show, at sub-mm wavelengths on years timescales, a $\sim 10\%$ peak to peak variability that can slightly affect the luminosity (Lee et al. 2021b; Mairs et al. 2024). Their mm dust emission is optically thick in the central region (Maury et al. 2019; Galametz et al. 2019; Li et al. 2017; Ko et al. 2020; Guerra-Alvarado et al. 2023) to completely obscure (for 4A1) or partially absorb (for 4A2) the mm iCOMs emission (De Simone et al. 2020). The two protostars emit large bipolar jet/outflows, deeply studied with several tracers, such as CO, SiO, SO, HCN and some iCOMs (including methanol; e.g., Lefloch et al. 1998; Choi et al. 2011; Ching et al. 2016; De Simone et al. 2020; Chuang et al. 2021). The southern lobes are blue-shifted, and the northern ones red-shifted and they cover a large velocity range (up to 60 km s^{-1} ; Choi 2005; Santangelo et al. 2015; Taquet et al. 2020). However, none of the previous studies resolve the inner 200 au (below $0''.7$). The FAUST data provide the superb spatial resolution of 50 au, that allows us to explore for the first time these inner regions using selected chemical tracers.

2. Observations

The observation of NGC 1333 IRAS 4A we present here are part of the Cycle 6 ALMA Large Program FAUST (PI. S. Yamamoto, 2018.1.01205.L). They were performed between October 2018 and September 2019 with baselines for the 12-m array between 15.1 m and 3.6 km. The bandpass and flux calibrator was J0237+2848, while J0336+3218 and J0328+3139 were used for the phase calibration. The map phase center is at R.A. (J2000) = 03h29m10s.539, Dec. (J2000) = $31^{\circ}13'30''.92$. For this work we used CH_3OH ($5_{1,4} - 4_{1,3}\text{A}$) and SiO ($5 - 4$) lines at 243.916 GHz and 217.105 GHz, respectively, in the high resolution spectral windows ($\Delta\nu = 0.123 \text{ kHz}$, corresponding to about 0.15 km s^{-1} and 0.17 km s^{-1} , for CH_3OH and SiO, respectively). The data were calibrated using the ALMA calibration pipeline within CASA² with an additional calibration routine to correct for the Tsys normalization issue³. After aligning data from different setups, phase-only self-calibration was performed on the continuum, generated using a careful manual detection of line-free channels. The continuum model was then subtracted from the visibilities prior to imaging the line data and a continuum image was then created in CASA. The resulting continuum-subtracted line cube was created combining the two available ALMA-12m configurations (i.e. C43-3, C43-6), to have the best angular resolution, and imaged with the IRAM-GILDAS⁴ package, using a 0.56 robust parameter⁵ with a resulting synthesized

beam of $0''.18 \times 0''.11$ (-13°) and $0''.14 \times 0''.096$ (-21°) for the SiO and CH_3OH spectral windows, respectively. The cubes were then primary beam corrected. We estimate the absolute flux error of 15% that includes the calibration uncertainty and an additional error for the spectra baseline determination.

3. The kinematical structure of the IRAS 4A inner regions

Figure 1 shows the dust continuum emission at 1.3 mm of NGC 1333 IRAS 4A overlaid with the SiO 5-4 low velocity emission (in the ranges $(-6, -2)$ and $(+2, +6) \text{ km s}^{-1}$ with respect to the v_{sys} ; $v_{\text{sys}} = 6.8 \text{ km s}^{-1}$; Choi 2001), with a zoom-in on SiO and CH_3OH emission lines (listed in Table 1) at $< 1''$ (< 300 au) scale around IRAS 4A2. At large scale (above $1''$ from IRAS 4A2, Figure A.1), both SiO and CH_3OH trace blue-shifted emission in the south (up to -33 km s^{-1} with respect to v_{sys}), and red-shifted emission in the north (up to $+35 \text{ km s}^{-1}$ with respect to v_{sys}). However, at small scales the kinematics is different: below 300 au, both SiO and CH_3OH emit in the velocity ranges $(-6, -2) \text{ km s}^{-1}$ and $(+2, +6) \text{ km s}^{-1}$ with respect to v_{sys} (see also channel maps in Figure B.1, and B.2) with a velocity gradient inverted with respect to the large scale. Specifically, CH_3OH shows blue-shifted emission towards the northeast and red-shifted emission towards the southwest, that peaks at $\sim 0''.15$ from IRAS 4A2 and extends out to $\sim 0''.3$. The SiO emission has an S-shape structure that follows the continuum emission from the dust grains in the circumstellar envelope. In the inner 300 au, it shows both blue- and red-shifted emission on both sides. However, in the inner $0''.3$ (~ 90 au) the SiO distribution resembles that of methanol, with an inverted velocity gradient with respect to the large scale emission. At larger distances, i.e. from $0''.3$ to $1''$, the southern lobe is only blue-shifted (in agreement with the large scale), while the northern lobe is mainly red-shifted with a tiny blue-shifted contamination (that dominates closer to the v_{sys} ; at about -2 km s^{-1} , Figure B.1). We also performed PV diagrams along the methanol and SiO PA and perpendicular to the emission (see Figure D.1, D.2, D.3). The inversion of velocity is clearly shown, but the PV diagrams are limited in spatial/angular resolution to reveal any other kinematical structure.

Figure 2 shows the spectra extracted at the position of the CH_3OH red- and blue-shifted emission peaks (coordinate offsets reported in Table 1). The two peaks were identified as the pixel with the highest flux level in the integrated maps of CH_3OH in the $(-6, -2) \text{ km s}^{-1}$ and $(+2, +6) \text{ km s}^{-1}$ ranges (see Figure 1). The CH_3OH spectrum peaks at low velocity ($\sim \pm 1.5 \text{ km s}^{-1}$ with respect to v_{sys}) and is likely dominated by the ice mantle sublimation region (i.e., the hot corino). The SiO spectrum, instead, peaks at higher velocity (about $\pm 7 \text{ km s}^{-1}$ with respect to v_{sys}) and it is likely dominated by jet/outflow emission due to grain sputtering/shattering. In the $(-6, -2) \text{ km s}^{-1}$ and $(+2, +6) \text{ km s}^{-1}$ ranges the spectra of CH_3OH and SiO overlap. In these ranges we observe the inverted velocity gradient. We measured the intensity ratio $\text{CH}_3\text{OH}/\text{SiO}$ (Table 1), integrated on the $(-6, -2) \text{ km s}^{-1}$ and $(+2, +6) \text{ km s}^{-1}$ ranges, and the corresponding abundance ratio, estimated assuming LTE (Local Thermodynamic Equilibrium) optically thin emission and an excitation temperature of 100 K (typical for both hot corino and shocked gas), in the red- and blue- shifted emission peaks of both SiO and CH_3OH . The emission peaks of SiO were identified, as for CH_3OH , as the pixel with the highest flux level in the integrated maps (Figure 1). We found that, in general, CH_3OH is more abundant than SiO by about two orders of magnitude. Additionally, the moment 0

² <https://casa.nrao.edu>

³ <https://help.almascience.org/kb/articles/what-are-the-amplitude-calibration-issues-caused-by-almas-normalization-strategy>

⁴ <https://www.iram.fr/IRAMFR/GILDAS/>

⁵ <https://www.iram.fr/IRAMFR/GILDAS/doc/pdf/map.pdf>

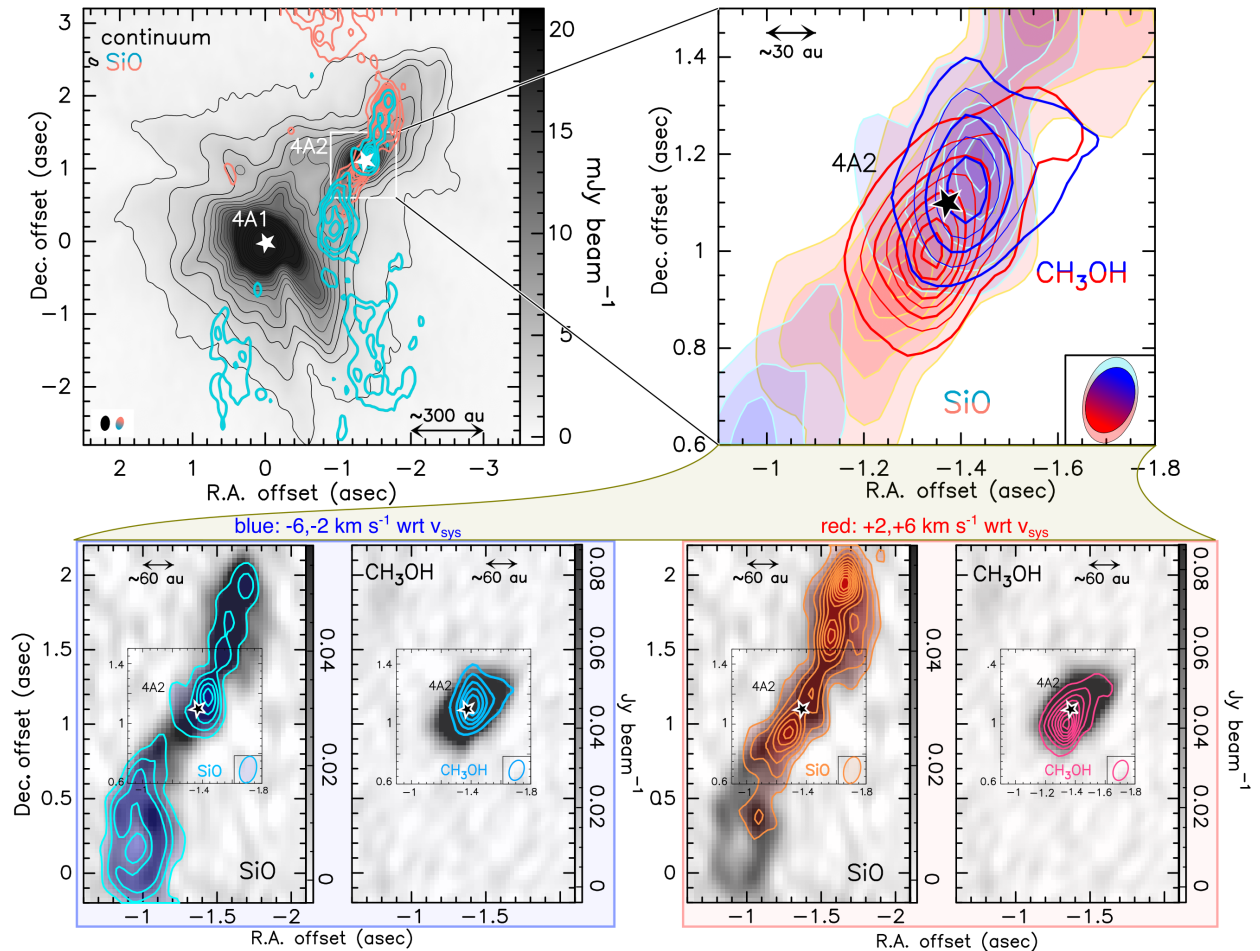


Fig. 1. *Upper left:* Superposition of the 1.3 mm continuum (grey scale, up to 20% of maximum flux, with contours starting at $15\sigma_c$ with step of $20\sigma_c$, where $\sigma_c = 8 \times 10^{-2} \text{ mJy beam}^{-1}$) with SiO red- and blue-shifted emission (salmon and cyan contours, respectively, from 3σ with steps of 4σ , where $\sigma = 2 \text{ mJy beam}^{-1} \text{ km s}^{-1}$). *Upper right:* Zoom-in on IRAS 4A2. Superposition of the red- and blue-shifted emission of SiO (salmon and cyan color shaded contours) and CH₃OH (red and blue contours). Contours starts at 3σ with steps of 4σ for SiO and 5σ for CH₃OH ($\sigma = 2 \text{ mJy beam}^{-1} \text{ km s}^{-1}$). Beams are shown in the lower corners. *Lower panels:* Blue- and red-shifted emission for SiO and CH₃OH shown separately. The beams are shown in the inner corner. In all panels, white (and black) stars mark the protostars (IRAS 4A1 and IRAS 4A2). The red- and blue-shifted emissions are integrated between $+2$ and $+6 \text{ km s}^{-1}$, and between -6 and -2 km s^{-1} with respect to the systemic velocity ($v_{\text{sys}} = +6.8 \text{ km s}^{-1}$; Choi 2001), respectively. The moment 0 between -6 and 6 km s^{-1} for each species is shown in greyscale.

maps in Figure 1 show that methanol peaks closer to the source than SiO in both blue and red ranges (by $0.1''$, less than a beam). Even if unresolved, this spatial shift in the red-shifted component seems to be significant. This is supported by the fact that the CH₃OH/SiO integrated intensity and abundance ratio estimated by extracting the spectra at the SiO peak are both about a factor 4 smaller than that estimated at the CH₃OH peak (Table 1). Finally, in IRAS 4A2 De Simone et al. (2020) estimated an H₂ density of about $2 \times 10^6 \text{ cm}^{-3}$ in the inner $0''.24$. Using this gas density, the abundances of CH₃OH and SiO are $\sim 10^{-6}$ and $\sim 10^{-8}$, respectively.

In summary, the observed emission arises from three zones: i) a very compact region ($< 0''.15$, $< 50 \text{ au}$), at $\pm 1.5 \text{ km s}^{-1}$ with respect to v_{sys} , dominated by the hot corino emission and traced mainly by methanol; ii) an intermediate region ($0''.15 - 0''.5$, $50 - 150 \text{ au}$), between 2 and 6 km s^{-1} with respect to v_{sys} , traced by both SiO and CH₃OH that shows an inverted velocity gradient, with respect to the large scale, whose origin is not clear; iii) an extended region ($> 0''.5$, $> 150 \text{ au}$), above 7 km s^{-1} with respect to the v_{sys} , traced by SiO and dominated by the jet/outflow.

4. On the origin of the inverse velocity gradient

We now discuss the origin of the intermediate region in the inner $\sim 0''.5$ ($\sim 150 \text{ au}$), where SiO and CH₃OH show an observed inverse velocity gradient with respect to the large scale, and their observed spatial and spectral shift. At this stage, it is important to highlight the formation mechanisms of these two species: CH₃OH is formed on the icy grain mantles via CO hydrogenation (e.g., Watanabe & Kouchi 2002; Rimola et al. 2014) and it can be released into gas phase by either ice mantle sublimation or by grain mantle sputtering in mild shocks in star forming regions (e.g., Flower et al. 2010). On the contrary, SiO is formed via the sputtering/shattering of the grain cores by strong shocks that release Si into the gas phase where it quickly oxygenates. It is estimated that up to $\sim 10\%$ of Si or SiO can also be frozen into the grain mantles, and therefore be released by grain mantle sputtering in mild shocks as CH₃OH (e.g., Caselli et al. 1997; Schilke et al. 1997; Gusdorf et al. 2008a,b; Guillet et al. 2011). Being the two species aligned along the same Position Angle (PA), it can be reasonable to think that they both come from from the base of the wind launched from the protostellar disk. However, CH₃OH is more compact and could also probe the very inner

Table 1. *Top:* Spectral properties of CH₃OH and SiO by Xu et al. (2008) and Müller et al. (2013), respectively, from the CDMS database (Müller et al. 2005). *Bottom:* Integrated Area in the blue (from 0.8 to 4.8 km s⁻¹) and red (from 8.8 to 12.8 km s⁻¹) velocity ranges from the spectra extracted at the blue- and red-shifted peaks of CH₃OH and SiO (see Figure 1 and 2) and corresponding column densities.

Line	Transition	Frequency [GHz]	E _u [K]	log(A _{ul} /s ⁻¹)	g _u	Beam " × " (°)		
SiO	5-4	217.10498	31	-3.28	11	0.18 × 0.11(-13)		
CH ₃ OH	5 _{1,4} - 4 _{1,3} A	243.91579	50	-4.22	44	0.14 × 0.096(-21)		
Velocity-integrated intensity (∫ IΔv) ^a & Column Density (N _{col}) ^b								
Position Offset ^c	CH ₃ OH Red Peak (-1'':35, +1'')		SiO Red Peak (-1'':27, +0'':93)		CH ₃ OH Blue Peak (-1'':41, +1'':13)		SiO Blue Peak (-1'':44, +1'':19)	
	∫ IΔv [K km s ⁻¹]	N _{col} [cm ⁻²]	∫ IΔv [K km s ⁻¹]	N _{col} [cm ⁻²]	∫ IΔv [K km s ⁻¹]	N _{col} [cm ⁻²]	∫ IΔv [K km s ⁻¹]	N _{col} [cm ⁻²]
SiO	44(6)	8.7(1.1)×10 ¹³	54(8)	10(2)×10 ¹³	51(8)	10(2)×10 ¹³	43(6)	8.5(1.1)×10 ¹³
CH ₃ OH	118(17)	37(5)×10 ¹⁵	37(6)	12(2)×10 ¹⁵	67(10)	21(3)×10 ¹⁵	52(8)	16(2)×10 ¹⁵
CH ₃ OH/SiO	∫ IΔv 2.7(0.8)	N _{col} 420(110)	∫ IΔv 0.7(0.2)	N _{col} 120(40)	∫ IΔv 1.3(0.4)	N _{col} 210(70)	∫ IΔv 1.2(0.3)	N _{col} 190(50)

^a Errors on the integrated intensity include 15% of calibration error and spectral baseline determination.

^b N_{col} has been computed assuming a T_{ex} of 100 K. A difference in T_{ex} of 50 K translates into about a factor 2 in N_{col}.

^c with respect to the map phase center.

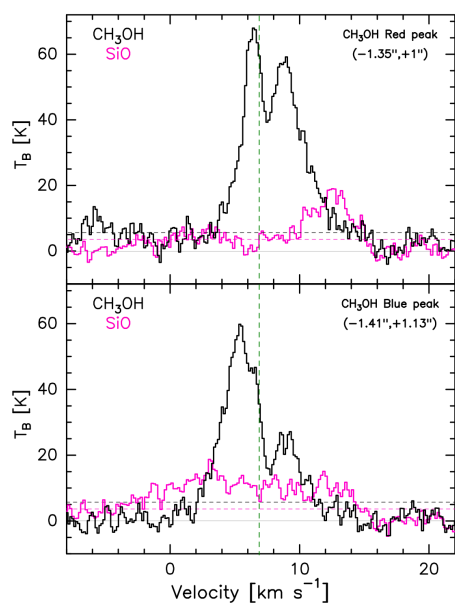


Fig. 2. SiO (magenta) and CH₃OH (black) spectra extracted at the blue- and red-shifted peaks of CH₃OH (offset with respect to the map phase center are in the upper right corner). The green dashed vertical line marks the v_{sys} (~6.8 km s⁻¹ Choi 2001). The 3σ level is reported in black (CH₃OH) and magenta (SiO) dashed horizontal lines.

part of the envelope where it is released by thermal evaporation. We investigate the following three possibilities:

Rotating disk/inner envelope: The blue- and red- shifted emission of CH₃OH might indicate rotation in a disk-like structure and/or in the inner envelope, where the ice sublimation dominates the chemistry. However, i) the PA (~ -30°) of the velocity gradient differs of ~ 30° from the perpendicular direction of the jet/outflow direction at large scale (above 300 au), as expected for disk emission. Indeed, the jet/outflow direction is estimated

to have a PA of 25° - 30° (see figure A.1, and Choi 2005; Santangelo et al. 2015; De Simone et al. 2020, Chahine et al. submitted); ii) unfortunately, the present spatial resolution (~ 50 au) is not enough to assess whether the signature of a rotating/infalling envelope is present in CH₃OH and/or SiO (see Figure D.2 in appendix); iii) CH₃OH and SiO are aligned on the same PA, and both trace the inverted velocity gradient, but only CH₃OH is a known disk tracer.

Indeed, while methanol emission can be explained by ice sublimation, for SiO is not so straightforward. At the methanol emission site (extending out to 90 au, 0'':3, and peaking at 45 au, 0'':15, from the protostar) the dust temperature is 65–90 K, comparable to the CH₃OH sublimation one (60–130 K) (see computations in Appendix C). On the other hand, SiO is usually associated to jet activity, i.e., where the Si is released by grain sputtering in shocks or entrained in a wind originated inside the dust sublimation radius (e.g., Cabrit et al. 2007; Gusdorf et al. 2008b; Hirota et al. 2017; Tabone et al. 2020; López-Vázquez et al. 2024). Even if there is 10% of SiO trapped in the ice mantles (e.g., Gusdorf et al. 2008a,b; Guillet et al. 2011), it is not clear if this would be released with the ice once sublimated due to SiO reactivity with water or due to other processes (see details in Appendix C). Alternatively, the two species could be released by grain mantle sputtering at the infalling envelope-disk interface, where slow shocks (< 5-10 km s⁻¹) occur (e.g., Sakai et al. 2014). However, it is unclear if this slow shocks can sputter enough SiO, and if so, the emission would follow the disk kinematics, for which we do not have strong evidence (see above).

In summary, the observed methanol emission could be the result of the ice mantle sublimation in the inner rotating envelope/disk, while a fast shock (>10 km s⁻¹) needs to occur to sputter the dust grains so to explain the observed SiO abundance.

Jet/Outflow precessing and/or on the plane of the sky: Another possibility is that CH₃OH and SiO have a non-thermal origin linked to shocks along the jet. The inclination of the IRAS 4A2 jet is yet highly uncertain Yıldız et al. (45°-88° 2012); Choi

(45°–88° 2005); Marvel et al. (45°–88° 2008); Koumpia et al. (45°–88° 2016). If it is close to the plane of the sky one expects to observe blue- and red-shifted emission in both lobes and along the whole jet length, not only in the inner 300 au (see e.g., Cabrit & Bertout 1990; Podio et al. 2021). On the other hand, if the jet precesses and crosses the plane of the sky it may create a knot with opposite velocity with respect to previous ejection events. However, if this was the case we would expect to see an alternation of blue- and red-shifted emission with a periodic pattern and also at larger scales. Moreover, this scenario has been excluded by Chuang et al. (2021) based on a 3D precession model. Indeed, this could explain the S-shape structure of the IRAS 4A outflows traced in SO at large scale, but not the inversion of the velocity gradient at small scales.

Wide-angle wind: Figure 3 shows a simplistic sketch that summarize our interpretation of the observed spatial-kinematical distribution. The sketch shows the base of a wide and inclined disk wind that crosses the plane of the sky and shows an inversion in velocity at 300 au with respect to the large-scale jet/outflow. The disk wind is plausibly magnetically driven and it is expected to reach the maximum radius at the Alfvén surface and to re-collimate beyond that (Tabone et al. 2020). The prototypical disk wind in HH212 has been detected at heights below ~ 200 au (Frank et al. 2014; Tabone et al. 2017; Lee et al. 2021a; Nazari et al. 2024), consistent with our findings. Given the covered velocity ranges between 2 and 6 km s⁻¹, the inclination of the gas crossing the plane of the sky has to be $> 55^\circ$ with respect to the line of sight. This is needed to have a reasonable flow velocity (> 10 km s⁻¹) to sputter grain mantles and cores so to release both CH₃OH and SiO (see Appendix C).

Among the three scenarios, we favour the last one as it explains the inverse velocity gradient, the spatial alignment between SiO and CH₃OH, and also the observed SiO and CH₃OH spectra (where the emission close to v_{sys} is hot corino dominated and beyond 7 km s⁻¹ is jet/outflow dominated). For the first time, we detect and identify a disk wind candidate toward the IRAS 4A Class 0 protostar traced in SiO and CH₃OH. This increases the number of disk wind tracers, complementing the typical SO (e.g., Tabone et al. 2017; Codella et al. 2018) and supporting the recently discovered CH₃OH (Nazari et al. 2024), and gives important constraints (velocity, inclination, and opening angles) for disk wind theories. It is important to notice that the emission of SiO can also be the result of the interaction of the jet with the disk wind giving rise to an unresolved shocked shell (see e.g., Lee et al. 2022b), or a disk wind rotation (e.g., Lee et al. 2022b). In this way, SiO can be considered as an indirect tracer. However, to explain the observed low velocities, the jet/wind inclination needs to be quite high (above 80° with respect to the line of sight; see Appendix C). Anyways, observations down to at least 10 au would be needed to test this scenario.

5. Conclusions

This Letter presents FAUST observations with 50 au resolution of IRAS 4A2 as mapped in SiO and CH₃OH. The high spatial and spectral resolution observation of FAUST have been crucial to study the interplay between the disk, the envelope and the outflowing gas. The unique combination of kinematics and chemistry allowed us to disentangle the emission at very small scales (50 au) using the chemical formation pathway of each species to retrieve the physical mechanisms at play. The emission below 300 au arises from three zones: i) a very compact region ($< 0''.1$,

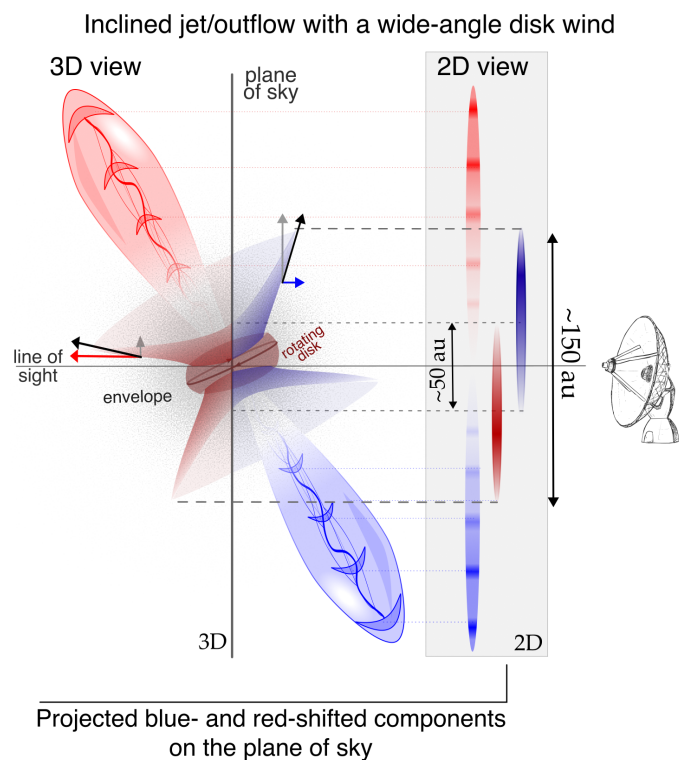


Fig. 3. Simplistic sketch (not in scale) of the proposed scenario: The large scale jet is quite inclined (60° in the example), and it has a wide outflowing shocking gas that crosses the plane of the sky. The red-shifted blue-shifted emission are represented by red and blue colors respectively. The gray-shadowed box highlight the view of the projected emission on the plane of the sky that we actually observe.

50 au), at ± 1.5 km s⁻¹ with respect to v_{sys} , dominated by the ice mantle sublimation zone and traced by methanol; ii) an intermediate region ($0''.1 - 0''.5$, 50–150 au), between 2 and 6 km s⁻¹ with respect to v_{sys} , traced by both SiO and CH₃OH that shows an inverted velocity gradient with respect to the large scale, with unknown origin; iii) an extended region ($> 0''.5$, 150 au), above 7 km s⁻¹ with respect to v_{sys} , traced by SiO and dominated by the outflow. We propose that CH₃OH and SiO in the intermediate region probe the base of a rotating wide-angle disk wind. The material accelerated in the wind crosses the plane of the sky, giving rise to the observed inverted velocity gradient, and sputter the grains releasing both species. For the first time we observe the IRAS 4A disk wind traced by, SiO and CH₃OH, new tracers beyond the known SO. Finally, we emphasise that observations down to 10 au will be essential to reveal the presence and the possible contribution of the unresolved rotating disk.

Acknowledgements: We warmly acknowledge Dr. J. Enrique Romero for the fruitful discussion on the binding energies and the Si, SiO insights, and Dr. F. Bacciotti on disk winds. This project has received funding from the Marie Skłodowska-Curie for the project “Astro-Chemical Origins” (ACO), grant agreement No 811312, and within the European Union’s Horizon 2020 research and innovation program from the European Research Council (ERC) for the projects “The Dawn of Organic Chemistry” (DOC), grant agreement No 741002. Part of the data deconvolution and analysis was performed using the GRICAD infrastructure (<https://gricad.univ-grenoble-alpes.fr>). CICO, LP, and GS acknowledge the PRIN-MUR 2020 BEYOND-2p (Astrochemistry be-

yond the second period elements, Prot. 2020AFB3FX), the PRIN MUR 2022 FOSSILS (Chemical origins: linking the fossil composition of the Solar System with the chemistry of protoplanetary disks, Prot. 2022JC2Y93), the project ASI-Astrobiologia 2023 MIGLIORA (Modeling Chemical Complexity, F83C23000800005), the INAF-GO 2023 fundings PROTO-SKA (Exploiting ALMA data to study planet forming disks: preparing the advent of SKA, C13C23000770005), the INAF Mini-Grant 2022 “Chemical Origins” (PI: L. Podio), and INAF-Minigrant 2023 TRIESTE (“TRacing the chemical hEritage of our originS: from proTostars to planEts”; PI: G. Sabatini). D.J. is supported by NRC Canada and by an NSERC Discovery Grant. L.L. acknowledges the support of DGAPA PAPIIT grants IN108324 and IN112820 and CONACyT-CF grant 263356”. M.B. acknowledges support from the European Research Council (ERC) Advanced Grant MOPPEX 833460. N.C acknowledges funding from the European Research Council (ERC) under the European Union Horizon Europe research and innovation program (grant agreement No. 101042275, project Stellar-MADE). This paper makes use of the following ALMA data: ADS/JAO.ALMA#2018.1.01205.L (PI: S. Yamamoto). ALMA is a partnership of the ESO (representing its member states), the NSF (USA) and NINS (Japan), together with the NRC (Canada) and the NSC and ASIAA (Taiwan), in cooperation with the Republic of Chile. The Joint ALMA Observatory is operated by the ESO, the AUI/NRAO, and the NAOJ.

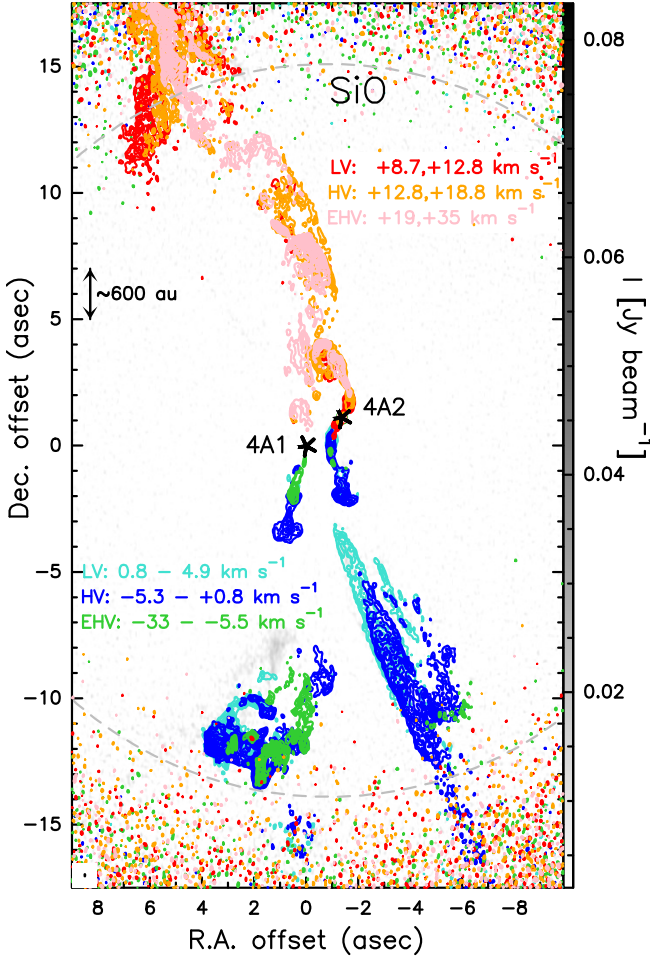


Fig. A.1. Large scale view of the ALMA FAUST SiO emission. Each velocity range corresponds to a specific color shown in contours starting at 4σ with steps of 2σ , where $\sigma = 3, 3.5, 6 \text{ mJy beam}^{-1} \text{ km s}^{-1}$ for the LV (low velocity: red and cyan), HV (high velocity: orange and blue), EHV (extremely high velocity: pink and green), respectively. In background, in grey scale, a range around the v_{sys} is shown ($4.9\text{--}8.5 \text{ km s}^{-1}$). The synthesised beam is depicted in the lower left corner, and the primary beam is shown as a dashed grey circle.

Appendix A: Overview of FAUST SiO at large scale

Figure A.1 shows the large scale SiO emission of the IRAS 4A system integrated in different velocity ranges. This provides a general overview of the whole range of velocities overall involved, for the sake of completeness. Please note that the SiO emission is actually going beyond the spectral window bandwidth, therefore beyond the upper velocity range value reported in the figure. It is important to note for the present work that the northern part is red-shifted and the southern part is blue-shifted. The study of the large scale structure is out of the scope of this letter and presented in Chahine et al. (submitted).

Appendix B: Channel maps

Figure B.1 and B.2 show the channel maps of SiO and CH₃OH, respectively. The channels are binned to 1 km s^{-1} , for the sake of clarity, and are zoomed in the inner 300 au of the IRAS 4A2 protostar. The inverted velocity gradient region is present only in the $(-6, -2)$ and $(2, 6) \text{ km s}^{-1}$ ranges.

Appendix C: SiO and CH₃OH: sputtering or sublimation?

Sublimation: In order to have the desorption of a species from the ice mantle, the dust needs to reach the species sublimation temperature. Considering species that are not strongly associated to each other (e.g. CH₃OH adsorbed on a surface made mostly by water or CO) the first order solution for the desorption rate (k_{des}) is:

$$k_{\text{des}} = v_{\text{des}} e^{-\text{BE}[K]/T}, \quad (\text{C.1})$$

where BE is the binding energy (namely, the strength of a species to remain attached to the surface) in Kelvin, and v_{des} is the pre-exponential factor which depends on the species and the surface (Minissale et al. 2022; Ferrero et al. 2022). Even if the BE is given most of the time as a single value, recent experiments and theoretical computations have shown that for each species there can be a distribution of BEs (Ferrero et al. 2020; Bovolenta et al. 2020; Minissale et al. 2022; Tinacci et al. 2022, 2023). This is because BE can change based on the site and orientation of the species with respect to the molecules on the substrate.

To retrieve the sublimation temperature from the desorption rate (i.e., the BE value) we solve Equation C.1 taking the half-life time $t_{1/2}$ as the characteristic time of the desorption, in first approximation, as (Ceccarelli et al. 2023):

$$t_{1/2} = \frac{\ln(2)}{k_{\text{des}}} = \frac{\ln(2)}{v_{\text{des}} e^{-\text{BE}[K]/T}}. \quad (\text{C.2})$$

Therefore,

$$T_{\text{sub}} = \frac{\text{BE}[K]}{\ln(t_{1/2}) + \ln(v_{\text{des}} / \ln(2))}. \quad (\text{C.3})$$

Regarding methanol, theoretical predictions by Ferrero et al. (2020) indicate a BE range of $(3770\text{--}8618) \text{ K}$, while the pre-exponential factor v_{des} is $3.2 \times 10^{17} \text{ s}^{-1}$ (Minissale et al. 2022). The BE given by Minissale et al. (2022) is 6621 K , consistent with the range found by Ferrero et al. (2020). Using the CH₃OH BE range and v_{des} stated above, and assuming that the grain mantles have been warmed up for a timescale of $\sim 10^4 \text{ yr}$ ⁶, $T_{\text{sub}} = 60\text{--}130 \text{ K}$.

We can now estimate the dust temperature at a certain distance from the protostar. When the dust is optically thin, the dust temperature profile heated by a central source with L_{\star} luminosity, can be approximated by the following equation (Ceccarelli et al. 2000):

$$T_{\text{dust}}[\text{K}] = 75 \text{ K} \left(\frac{L_{\star}}{27 L_{\odot}} \right)^{1/4} \left(\frac{r}{150 \text{ au}} \right)^{-1/2}. \quad (\text{C.4})$$

The bolometric luminosity (L_{bol}) of IRAS 4A1 and IRAS 4A2 is not measured singularly due to the lack of angular resolution observation at infrared wavelengths. The total bolometric luminosity of the IRAS 4A1+4A2 system is estimated to be $9 L_{\odot}$ (Kristensen et al. 2012; Karska et al. 2013). The blue- and red-shifted emission peak of methanol are separated by about $0''.15$ (about 45 au) and their emission extend up to $0''.26$ away (about 80 au). If we consider for 4A2 conservatively a bolometric luminosity of $4.5 L_{\odot}$ (half of the total luminosity), the temperature at 80 au from the protostars is about 65 K, while at 45 au is about 90 K.

⁶ Please note that assuming 1 Myr timescale, T_{sub} could be lower by about 10 K.

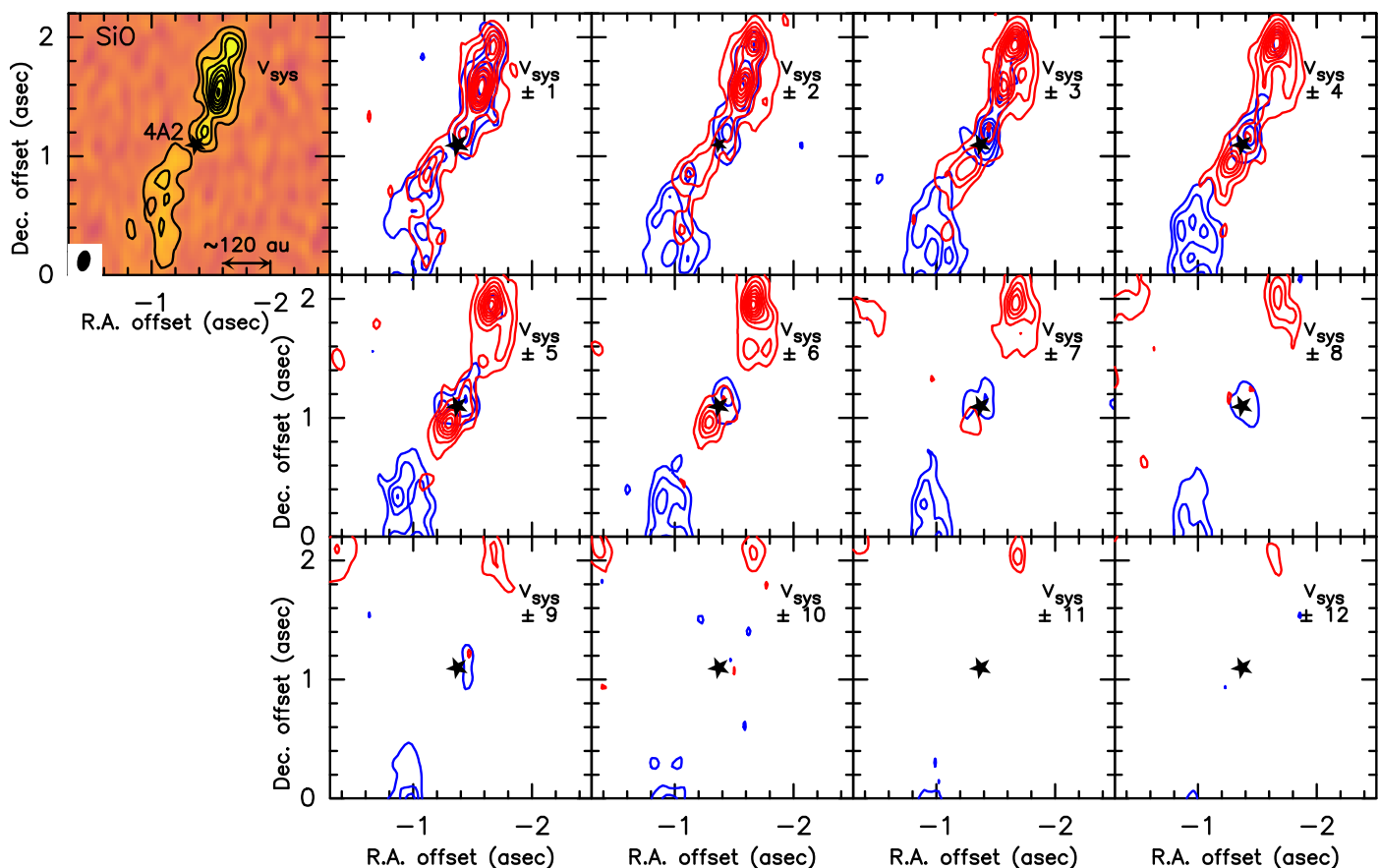


Fig. B.1. ALMA FAUST SiO velocity channel maps. Each panel corresponds to a 1 km s^{-1} increment from the systemic velocity ($v_{\text{sys}} = 6.8 \text{ km s}^{-1}$; Choi 2001). The black star marks the position of the IRAS 4A2 protostar. The SiO beam is reported in the lower left corner of the v_{sys} panel (shown in color scale). First contours and steps are 3σ ($\sigma = 1 \text{ mJy beam}^{-1}$).

Regarding SiO, it could be possible to investigate if sublimation can play a role, given that it is thought that about 10% of SiO can be already formed and locked into the ice mantles of the dust grains (see e.g., Gusdorf et al. 2008a,b; Guillet et al. 2011). The binding energy of SiO is reported to be about 3500 K (Hasegawa & Herbst 1993), that translate into a sublimation temperature of about 50 K. Therefore, in theory, at $0''.2$ (60 au) away from the protostar (at SiO emission peak), the dust temperature could be enough to sublimate SiO. If we consider the computed $\text{CH}_3\text{OH}/\text{SiO}$ column density ratio (see Table 1), we find that the abundances of SiO should be two order of magnitude lower than methanol. In IRAS 4A2, De Simone et al. (2020) estimated a gas density of about $2 \times 10^6 \text{ cm}^{-3}$ in the inner $0''.24$. Using this gas density, the abundances should be about 10^{-6} for CH_3OH and 10^{-8} for SiO (similar to the typical values in shocked regions; e.g., Cabrit et al. 2007; Gusdorf et al. 2008b; Taquet et al. 2020). Considering a 10% of elemental silicon frozen into SiO on the mantle, we could have an abundance of frozen SiO or Si on the icy mantle of about $10^{-7} - 10^{-8}$ (see Figure 4 in Ceccarelli et al. 2018; Lodders 2019). Therefore, we could, in principle, explain the observed abundance. However, SiO and Si could be highly reactive with the water molecules in the ice preventing the sublimation of pure SiO and Si into the gas phase. New quantum chemical computations are ongoing to obtain i) updated values for the SiO binding energy taking into account orientation and ice morphology (Gelli et al. in prep.), and ii) evaluating how much reactive the SiO and Si are on interstellar ices (Enrique-Romero et al. private comm.).

Sputtering: SiO is the best known and most studied shock tracers since more than two decades. Several shock models have predicted that the SiO abundance is highly enhanced in high velocity shocks (above 25 km s^{-1}). Indeed at these velocities the silicon is liberated from the refractory cores of the grains thanks to sputtering and/or shattering, and goes into the gas phase where it quickly oxidizes (e.g., Flower & Pineau des Forets 1994; Caselli et al. 1997; Schilke et al. 1997). At lower velocities, some species (including Si, directly SiO, and also CH_3OH) that were previously frozen on to the grain mantles can still be released into the gas phase by the sputtering of the icy mantles itself (Jiménez-Serra et al. 2008; Gusdorf et al. 2008b; Guillet et al. 2011; Lesaffre et al. 2013; Nguyen-Lu'o'ng et al. 2013). The above models predict that, to liberate Si or SiO from the frozen mantles, a minimum velocity of about 10 km s^{-1} is needed⁷.

From our observations, the small scale inverse velocity component has a velocity range between 2 and 6 km s^{-1} (see Figure 1, B.1, B.2). This represent the line-of-sight velocity component. To retrieve the radial velocity, that would be the responsible for the sputtering, we need information on the jet/outflow inclination. The IRAS 4A jet inclination is not very well known yet. Indeed, due to the large extent of the outflows/jets and the high line-of-sight velocities Yıldız et al. (2012) suggested an inclination of $45 - 60^\circ$ with respect to the line of sight. On the other hand, Choi (2005), Marvel et al. (2008), and Koumpia et al.

⁷ Please note that these values critically depend on the assumed frozen-SiO sputtering threshold energy (see discussion in De Simone et al. 2022b; Flower & Pineau des Forets 1994)

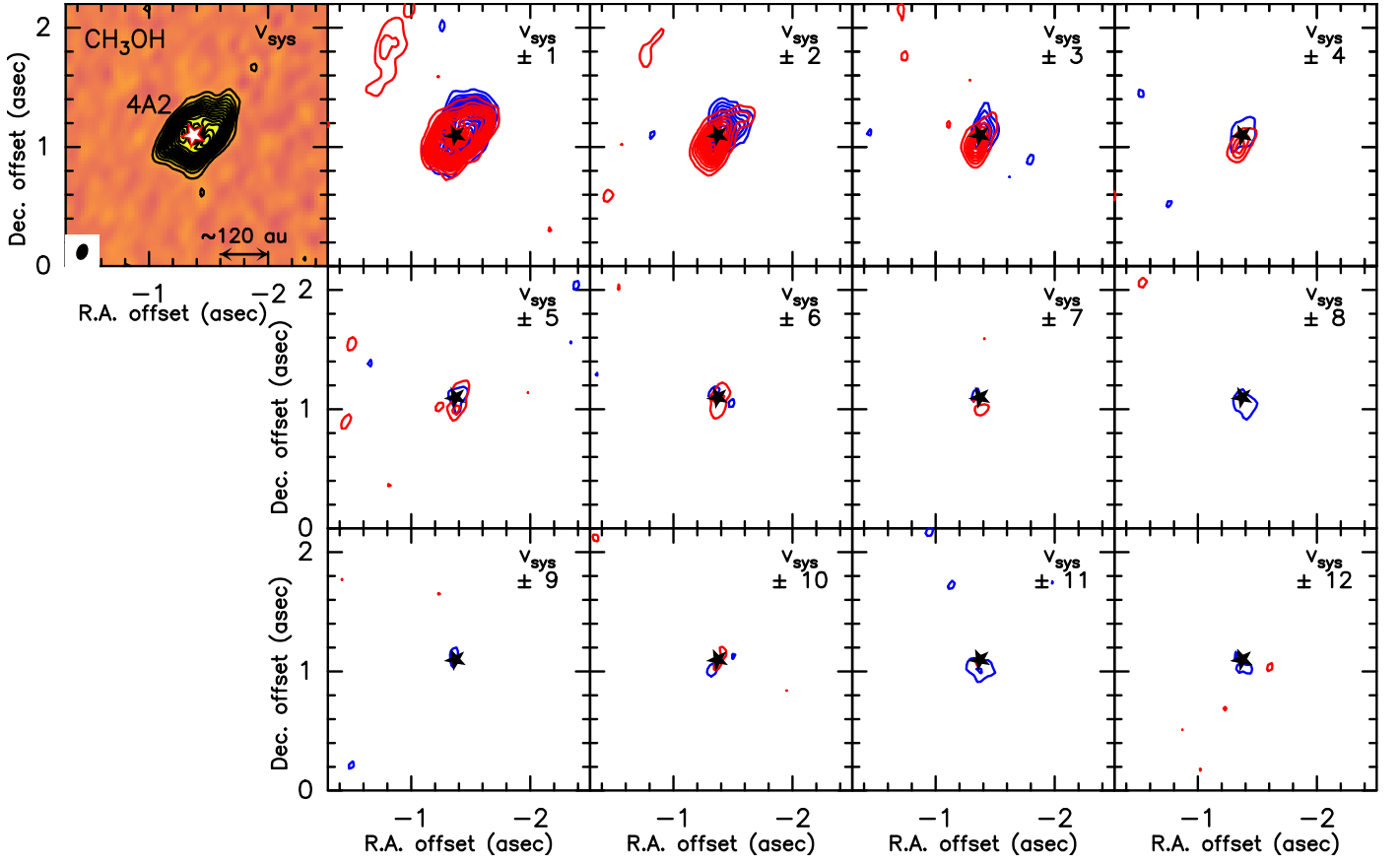


Fig. B.2. ALMA FAUST CH₃OH velocity channel maps. Each panel corresponds to a 1 km s⁻¹ increment from the systemic velocity ($v_{\text{sys}} = 6.8$ km s⁻¹; Choi 2001). The black star marks the position of the IRAS 4A2 protostar. The CH₃OH beam is reported in the lower left corner of the v_{sys} panel (shown in color scale). First contours and steps are 3σ ($\sigma = 1.1$ mJy beam⁻¹).

(2016) suggested larger inclination of about 79°, 88° and 70°, respectively. However, we can give a constrain on the inclination of the emission at this scale (not necessarily of the jet, see discussion in Section 4) based on the minimum velocity needed to have sputtering, so to explain the presence of both SiO and CH₃OH. Considering that the observed line-of-sight velocity is 2, 6 km s⁻¹ with respect to the v_{sys} , and the velocity required for sputtering a reasonable amount of SiO and CH₃OH (see above), we need an inclination with respect to the line of sight above 55° for a radial velocity of 10 km s⁻¹, and above 80° for 35 km s⁻¹.

Appendix D: PV Diagrams

We selected eight regions 0''.1 wide (shown in Figure D.1) where to extract the PV diagrams: one of 3''.6 length passing through the direction identified by the red- and blue-shifted emission peak of methanol in the inner 0''.5 (PA~30°) and the other seven are perpendicular to that, each separated by 0''.3, and of 1''.6 length. The PV diagrams extracted from these regions for SiO are shown in Figure D.3, while the one extracted from the parallel slice and the path following the SiO structures (shown in red and white, respectively, in Figure D.1) for both CH₃OH and SiO are shown in Figure D.2. It is possible to notice, as also visible in the channel maps (Figure B.1), that the SiO PV diagram on the path 0''.9 and 0''.6 south of IRAS 4A2 are blue-shifted while 0''.3 south a red-shifted component appears together with the blue-shifted ones. In the north paths the situation is similar with red and blue-shifted inverted. The emission is confined around $\pm 0''.3$ of the selected axis, and does not show any peculiar structure.

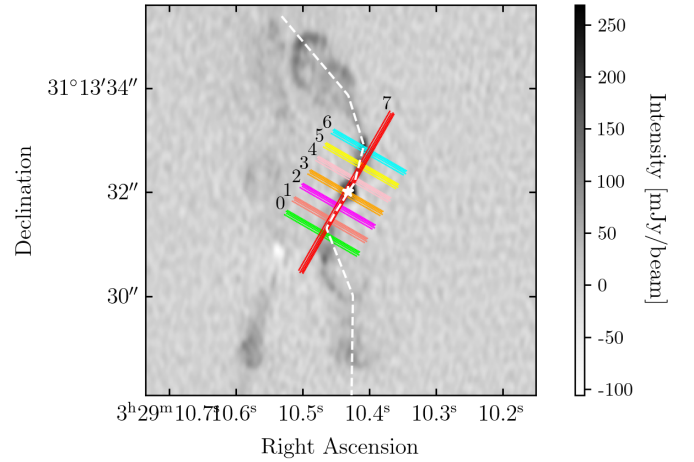


Fig. D.1. Regions (colored) where PV diagrams have been extracted. For reference, the moment 0 of SiO integrated over the whole spectral window is in grey scale. IRAS 4A2 is marked by the white star.

Only the emission along the path 0''.9 south of 4A2, that correspond to the cavity seen in the southern outflow (see Figure 1), is resolved and shows higher velocities with respect to the small scale structures (below 0''.5). In Figure D.2, the emission along the slice parallel to CH₃OH and SiO PA (red in Figure D.1) of SiO shows a more evident structure. It is noticeable the inversion of velocity gradient, with red emission in the south and blue emission in the north, below 0''.5 from 4A2. The knot at -0''.5

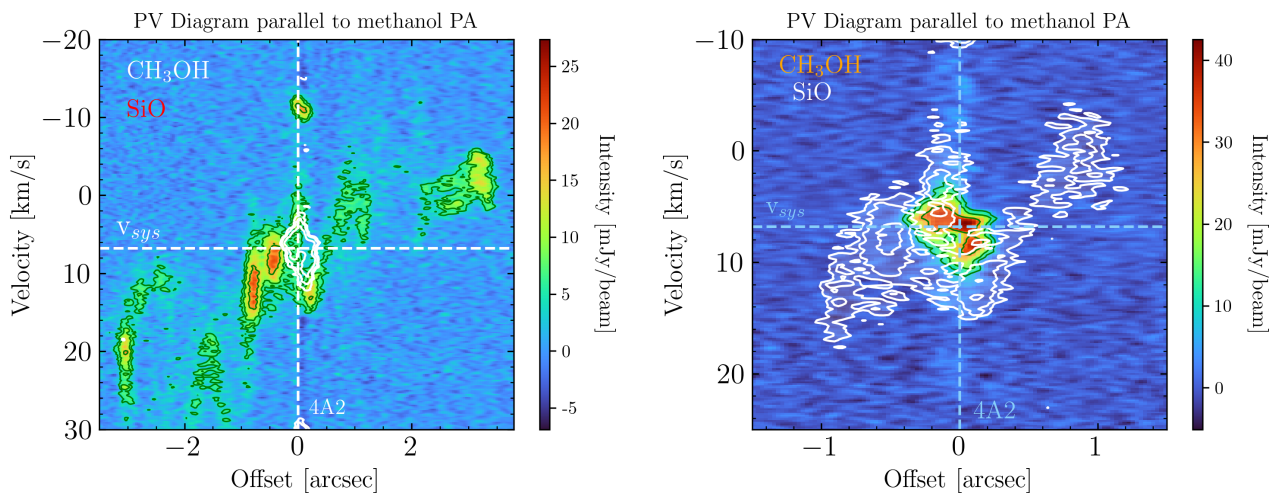


Fig. D.2. *Left:* PV Diagram extracted over the path of $\sim 7''$ length that follows the SiO structures (white in Figure D.1). The SiO emission is shown in color scale. Green and white contours at $(3,5,10) \sigma$ are for CH_3OH ($\sigma \sim 2 \text{ mJy beam}^{-1}$) and SiO ($\sigma_m \sim 1.6 \text{ mJy beam}^{-1}$), respectively. *Right* PV Diagram extracted over the region of $3''$ length passing through methanol and SiO PA in the inner $0''.5$ (shown in red in the left panel). The methanol emission is shown in color scale with green contours (at $3,5,10 \sigma_m$ with $\sigma_m \sim 3 \text{ mJy beam}^{-1}$). The SiO emission is shown in white contours at $(3,5,10, 20) \sigma_s$ with $\sigma_s \sim 1.5 \text{ mJy beam}^{-1}$. In both panels, the vertical and horizontal dashed lines represent the v_{sys} ($\sim 6.8 \text{ km s}^{-1}$; Choi 2001), and the $0''$ offset (on the 4A2 protostar), respectively.

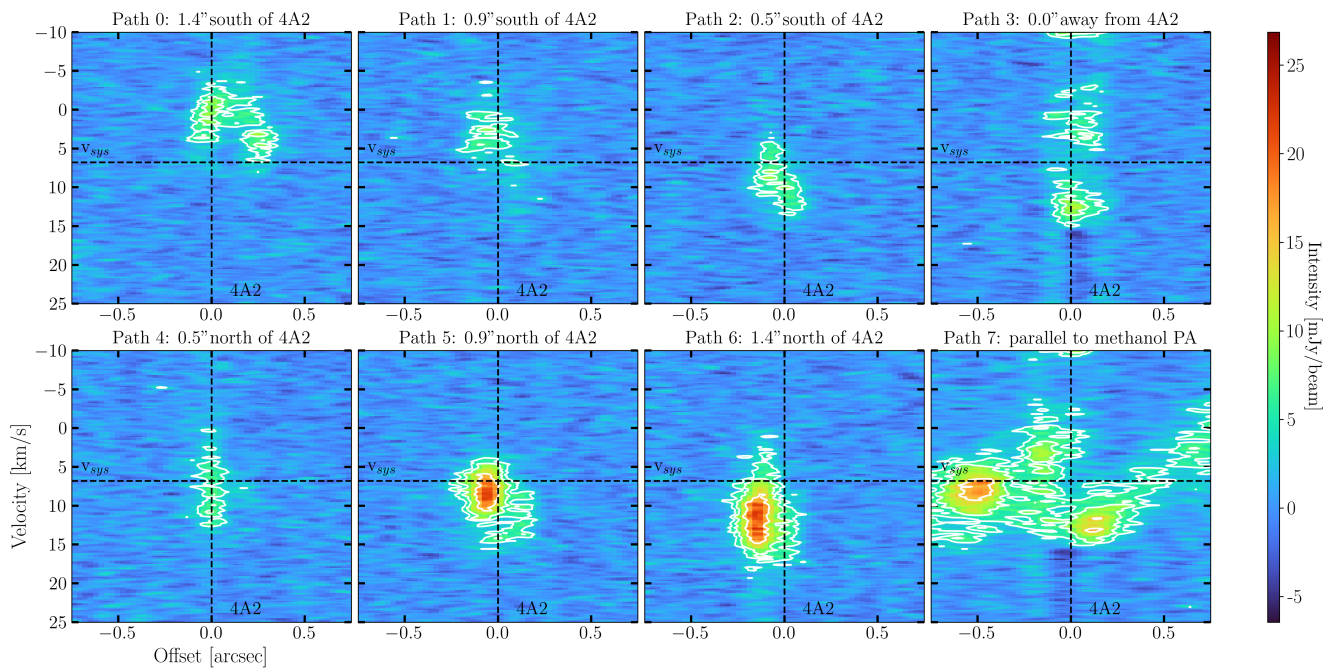


Fig. D.3. SiO PV diagrams extracted at the region shown in Figure D.1 and opportunely labelled at the top of each plot. The contours are at $(3,5,10, 20) \sigma_s$ with $\sigma_s \sim 1.5 \text{ mJy beam}^{-1}$. The vertical and horizontal dashed lines represent the v_{sys} ($\sim 6.8 \text{ km s}^{-1}$; Choi 2001), and the $0''$ offset (on the 4A2 protostar), respectively.

can be interpreted as the first knot associated to the outflow. Indeed, the left panel of the figure shows the PV diagram extracted from a region that follows the SiO structure in the moment 0 (white line in Figure D.1). Here two knots are at $\sim 0''.5$ and $\sim 1''$ with 8.5 km s^{-1} and 12 km s^{-1} respectively and indicate knots in the outflow. Comparing SiO and CH_3OH in Figure D.2 right), we can see that CH_3OH is elongated following the SiO emission with inverted velocity gradient. However, we are limited by spatial resolution to reveal any other kinematical structure.

References

- Andre, P., Ward-Thompson, D., & Barsony, M. 2000, PPIV, 59
Arce, H. G., Shepherd, D., Gueth, F., et al. 2007, in Protostars and Planets V, ed. B. Reipurth, D. Jewitt, & K. Keil, 245
Belloche, A., Maury, A. J., Maret, S., et al. 2020, arXiv:2002.00592 [astro-ph], arXiv: 2002.00592
Bianchi, E., López-Sepulcre, A., Ceccarelli, C., et al. 2023, Faraday Discussions, 245, 164
Blandford, R. D. & Payne, D. G. 1982, MNRAS, 199, 883
Bouvier, M., Ceccarelli, C., López-Sepulcre, A., et al. 2022, ApJ, 929, 10
Bovolenta, G., Bovino, S., Vöhringer-Martinez, E., et al. 2020, Molecular Astrophysics, 21, 100095
Cabrit, S. & Bertout, C. 1990, ApJ, 348, 530

- Cabrit, S., Codella, C., Gueth, F., et al. 2007, *A&A*, 468, L29
- Caselli, P., Hartquist, T. W., & Havnes, O. 1997, *A&A*, 322, 296
- Ceccarelli, C. 2004, in *ASPC*, Vol. 323, 195
- Ceccarelli, C., Caselli, P., Fontani, F., et al. 2017, *ApJ*, 850, 176
- Ceccarelli, C., Castets, A., Caux, E., et al. 2000, *A&A*, 355, 1129
- Ceccarelli, C., Codella, C., Balucani, N., et al. 2023, in *Astronomical Society of the Pacific Conference Series*, Vol. 534, *Protostars and Planets VII*, ed. S. Inutsuka, Y. Aikawa, T. Muto, K. Tomida, & M. Tamura, 379
- Ceccarelli, C., Viti, S., Balucani, N., & Taquet, V. 2018, *MNRAS*, 476, 1371
- Ching, T.-C., Lai, S.-P., Zhang, Q., et al. 2016, *ApJ*, 819, 159
- Choi, M. 2001, *ApJ*, 553, 219
- Choi, M. 2005, *ApJ*, 630, 976
- Choi, M., Kang, M., Tatematsu, K., Lee, J.-E., & Park, G. 2011, *Publications of the Astronomical Society of Japan*, 63, 1281
- Chuang, C.-Y., Aso, Y., Hirano, N., Hirano, S., & Machida, M. N. 2021, *ApJ*, 916, 82
- Codella, C., Bianchi, E., Tabone, B., et al. 2018, *A&A*, 617, A10
- Codella, C., Ceccarelli, C., Chandler, C., et al. 2021, *Frontiers in Astronomy and Space Sciences*, 8, 227
- De Simone, M., Ceccarelli, C., Codella, C., et al. 2020, *ApJL*, 896, L3
- De Simone, M., Ceccarelli, C., Codella, C., et al. 2022a, *ApJ*, 935, L14
- De Simone, M., Codella, C., Ceccarelli, C., et al. 2022b, *MNRAS*, 512, 5214
- De Simone, M., Codella, C., Ceccarelli, C., et al. 2020, *A&A*, 640, A75
- De Simone, M., Codella, C., Testi, L., et al. 2017, *A&A*, 599, A121
- de Valon, A., Dougados, C., Cabrit, S., et al. 2020, *A&A*, 634, L12
- Ferrero, S., Grieco, F., Ibrahim Mohamed, A. S., et al. 2022, *MNRAS*, 516, 2586
- Ferrero, S., Zamirri, L., Ceccarelli, C., et al. 2020, *ApJ*, 904, 11
- Flower, D. R. & Pineau des Forêts, G. 1994, *MNRAS*, 268, 724
- Flower, D. R., Pineau des Forêts, G., & Rabli, D. 2010, *MNRAS*, 409, 29
- Frank, A., Ray, T. P., Cabrit, S., et al. 2014, in *Protostars and Planets VI*, ed. H. Beuther, R. S. Klessen, C. P. Dullemond, & T. Henning, 451–474
- Galametz, M., Maury, A. J., Valdivia, V., et al. 2019, *A&A*, 632, A5
- Guerra-Alvarado, O. M., van der Marel, N., Di Francesco, J., et al. 2023, *arXiv e-prints*, arXiv:2310.11999
- Guillet, V., Pineau Des Forêts, G., & Jones, A. P. 2011, *A&A*, 527, A123
- Gusdorf, A., Cabrit, S., Flower, D. R., & Pineau Des Forêts, G. 2008a, *A&A*, 482, 809
- Gusdorf, A., Pineau Des Forêts, G., Cabrit, S., & Flower, D. R. 2008b, *A&A*, 490, 695
- Hasegawa, T. I. & Herbst, E. 1993, *MNRAS*, 261, 83
- Herbst, E. & Van Dishoeck, E. 2009, *ARA&A*, 47, 427
- Hirota, T., Machida, M. N., Matsushita, Y., et al. 2017, *Nature Astronomy*, 1, 0146
- Jiménez-Serra, I., Caselli, P., Martín-Pintado, J., & Hartquist, T. W. 2008, *A&A*, 482, 549
- Karska, A., Herczeg, G. J., van Dishoeck, E. F., et al. 2013, *A&A*, 552, A141
- Ko, C.-L., Liu, H. B., Lai, S.-P., et al. 2020, *ApJ*, 889, 172
- Konigl, A. & Pudritz, R. E. 2000, in *Protostars and Planets IV*, ed. V. Mannings, A. P. Boss, & S. S. Russell, 759
- Koumpia, E., van der Tak, F. F. S., Kwon, W., et al. 2016, *A&A*, 595, A51
- Kristensen, L. E., van Dishoeck, E. F., Bergin, E. A., et al. 2012, *A&A*, 542, A8
- Lee, C.-F., Codella, C., Ceccarelli, C., & López-Sepulcre, A. 2022a, *ApJ*, 937, 10
- Lee, C.-F., Li, Z.-Y., Shang, H., & Hirano, N. 2022b, *ApJ*, 927, L27
- Lee, C.-F., Tabone, B., Cabrit, S., et al. 2021a, *ApJ*, 907, L41
- Lee, Y.-H., Johnstone, D., Lee, J.-E., et al. 2021b, *ApJ*, 920, 119
- Lefloch, B., Castets, A., Cernicharo, J., & Loinard, L. 1998, *ApJ*, 504, L109
- Lesaffre, P., Pineau des Forêts, G., Godard, B., et al. 2013, *A&A*, 550, A106
- Li, J. I.-H., Liu, H. B., Hasegawa, Y., & Hirano, N. 2017, *ApJ*, 840, 72
- Lodders, K. 2019, *arXiv e-prints*, arXiv:1912.00844
- Looney, L. W., Mundy, L. G., & Welch, W. J. 2000, *ApJ*, 529, 477
- López-Vázquez, J. A., Lee, C.-F., Fernández-López, M., et al. 2024, *ApJ*, 962, 28
- Louvet, F., Dougados, C., Cabrit, S., et al. 2018, *A&A*, 618, A120
- López-Sepulcre, A., Sakai, N., Neri, R., et al. 2017, *A&A*, 606, A121
- Mairs, S., Lee, S., Johnstone, D., et al. 2024, *arXiv e-prints*, arXiv:2401.03549
- Marvel, K. B., Wilking, B. A., Claussen, M. J., & Wootten, A. 2008, *ApJ*, 685, 285
- Maureira, M. J., Gong, M., Pineda, J. E., et al. 2022, *ApJ*, 941, L23
- Maury, A. J., André, P., Testi, L., et al. 2019, *A&A*, 621, A76
- Minissale, M., Aikawa, Y., Bergin, E., et al. 2022, *ACS Earth and Space Chemistry*, 6, 597
- Müller, H. S. P., Spezzano, S., Bizzocchi, L., et al. 2013, *Journal of Physical Chemistry A*, 117, 13843
- Müller, H. S. P., Schlöder, F., Stutzki, J., & Winnewisser, G. 2005, *Journal of Molecular Structure*, 742, 215
- Nazari, P., Tabone, B., Ahmadi, A., et al. 2024, *arXiv e-prints*, arXiv:2402.18631
- Nguyen-Lu’o’ng, Q., Motte, F., Carloff, P., et al. 2013, *ApJ*, 775, 88
- Okoda, Y., Oya, Y., Imai, M., et al. 2022, *ApJ*, 935, 136
- Pascucci, I., Cabrit, S., Edwards, S., et al. 2023, in *Astronomical Society of the Pacific Conference Series*, Vol. 534, *Protostars and Planets VII*, ed. S. Inutsuka, Y. Aikawa, T. Muto, K. Tomida, & M. Tamura, 567
- Podio, L., Tabone, B., Codella, C., et al. 2021, *A&A*, 648, A45
- Ray, T., Dougados, C., Bacciotti, F., Eisloffel, J., & Chrysostomou, A. 2007, in *Protostars and Planets V*, ed. B. Reipurth, D. Jewitt, & K. Keil, 231
- Rimola, A., Taquet, V., Ugliengo, P., Balucani, N., & Ceccarelli, C. 2014, *A&A*, 572, A70
- Sakai, N., Oya, Y., Sakai, T., et al. 2014, *ApJ*, 791, L38
- Santangelo, G., Codella, C., Cabrit, S., et al. 2015, *A&A*, 584, A126
- Schilke, P., Walmsley, C. M., Pineau des Forêts, G., & Flower, D. R. 1997, *A&A*, 321, 293
- Shang, H., Li, Z. Y., & Hirano, N. 2007, in *Protostars and Planets V*, ed. B. Reipurth, D. Jewitt, & K. Keil, 261
- Shu, F., Najita, J., Ostriker, E., et al. 1994, *ApJ*, 429, 781
- Shu, F. H., Adams, F. C., & Lizano, S. 1987, *ARA&A*, 25, 23
- Tabone, B., Cabrit, S., Bianchi, E., et al. 2017, *A&A*, 607, L6
- Tabone, B., Cabrit, S., Pineau des Forêts, G., et al. 2020, *A&A*, 640, A82
- Taquet, V., Codella, C., de Simone, M., et al. 2020, *arXiv e-prints*, 2002, arXiv:2002.05480
- Tinacci, L., Germain, A., Pantaleone, S., et al. 2023, *ApJ*, 951, 32
- Tinacci, L., Germain, A., Pantaleone, S., et al. 2022, *ACE ECS*, arXiv e-prints, arXiv:2205.11954
- Tobin, J. J., Looney, L. W., Li, Z.-Y., et al. 2018, *ApJ*, 867, 43
- Tsukamoto, Y., Maury, A., Commerçon, B., et al. 2022, *arXiv e-prints*, arXiv:2209.13765
- Watanabe, N. & Kouchi, A. 2002, *ApJ*, 571, L173
- Xu, L.-H., Fisher, J., Lees, R. M., et al. 2008, *Journal of Molecular Spectroscopy*, 251, 305
- Yang, Y.-L., Evans, II, N. J., Smith, A., et al. 2020, *arXiv e-prints*, 2002, arXiv:2002.01478
- Yıldız, U. A., Kristensen, L. E., van Dishoeck, E. F., et al. 2012, *A&A*, 542, A86
- Zhang, Y., Higuchi, A. E., Sakai, N., et al. 2018, *ApJ*, 864, 76
- Zucker, C., Schlawly, E. F., Speagle, J. S., et al. 2018, *ApJ*, 869, 83

- 1 ESO, Karl Schwarzschild Str. 2, 85478 Garching bei München, Germany
e-mail: marta.desimone@eso.org
- 2 INAF, Osservatorio Astrofisico di Arcetri, Largo E. Fermi 5, 50125 Firenze, Italy
- 3 Univ. Grenoble Alpes, CNRS, IPAG, 38000 Grenoble, France
- 4 National Radio Astronomy Observatory⁸, 1003 Lopezville Rd, Socorro, NM 87801, USA
- 5 Institut de Radioastronomie Millimétrique (IRAM), 300 rue de la Piscine, 38406 Saint-Martin-d’Hères, France
- 6 Instituto de Radioastronomía y Astrofísica, Universidad Nacional Autónoma de México, A.P. 3-72 (Xangari), 8701, Morelia, Mexico
- 7 Instituto de Astronomía, Universidad Nacional Autónoma de México, Ciudad Universitaria, A.P. 70-264, Ciudad de México 04510, Mexico
- 8 The Institute of Physical and Chemical Research (RIKEN), 2-1, Hirosawa, Wako-shi, Saitama 351-0198, Japan
- 9 NRC Herzberg Astronomy and Astrophysics, 5071 West Saanich Road, Victoria, BC, V9E 2E7, Canada
- 10 Department of Physics and Astronomy, University of Victoria, Victoria, BC, V8P 5C2, Canada
- 11 Department of Astronomy, The University of Tokyo, 7-3-1 Hongo, Bunkyo-ku, Tokyo 113-0033, Japan
- 12 Leiden Observatory, Leiden University, P.O. Box 9513, 2300 RA Leiden, The Netherlands
- 13 IRAP, Université de Toulouse, CNRS, CNES, UPS, Toulouse, France
- 14 Excellence Cluster ORIGINS, Boltzmannstraße 2, 85748, Garching bei München, – Germany
- 15 Center for Astrochemical Studies, Max-Planck-Institut für extraterrestrische Physik (MPE), Gießenbachstr. 1, D-85741 Garching, Germany
- 16 Centre for Frontier Science, Chiba University, 1-33 Yayoi-cho, Inage-ku, Chiba 263-8522, Japan
- 17 Department of Chemistry, University of Virginia, McCormick Road, PO Box 400319, Charlottesville, VA 22904, USA
- 18 The University of Texas at Austin, 2515 Speedway, Austin, Texas 78712, USA
- 19 The Graduate University for Advanced Studies (SOKENDAI), Shonan Village, Hayama, Kanagawa 240-0193, Japan

⁸ The National Radio Astronomy Observatory is a facility of the National Science Foundation operated under cooperative agreement by Associated Universities, Inc.